Analysis of shear strain imaging for classifying breast masses: Finite element and phantom results

Haiyan Xu and Tomy Varghese[a)]
Department of Medical Physics, University of Wisconsin - Madison and Department of Electrical and Computer Engineering, University of Wisconsin-Madison, Madison, Wisconsin 53706

Ernest L. Madsen
Department of Medical Physics, University of Wisconsin-Madison, Madison, Wisconsin 53706

(Received 17 June 2011; revised 23 August 2011; accepted for publication 8 September 2011; published 24 October 2011)

Purpose: Features extracted from axial-shear strain images of breast masses have been previously utilized to differentiate and classify benign from malignant breast masses. In this paper, we compare shear strain patterns exhibited by both the full-shear (axial and lateral component) versus only the axial-shear strain component for differentiating between bound masses (malignant) when compared to unbound masses (benign).
Methods: We examine different breast mass characteristics such as mass shape, asymmetric location of masses, stiffness variations, and mass bonding characteristics to background tissue to assess their impact on shear strain patterns generated due to a uniaxial applied deformation. Two-dimensional finite element simulations of both circular and elliptical inclusions embedded within a uniform background were utilized. Different degrees of bonding were characterized using friction coefficient values ranging from 0.01 to 100 denoting loosely bound to firmly bound masses. Single-inclusion tissue-mimicking phantoms mimicking firmly bound and loosely bound ellipsoidal masses oriented at four different angles to the applied deformation were studied to corroborate the mass differentiation performance.
Results: Our results indicate that the normalized axial-shear strain and full-shear strain area features are larger for bound when compared to unbound masses. A higher stiffness ratio or contrast between the inclusion and background also improves differentiation. Larger applied deformations reduce the discrimination performance for masses with friction coefficients lower than 0.4, due to increased mass slippage with applied deformations. Potential errors with the use of these features would occur for unbound inclusions at larger applied deformations and for asymmetric mass positions within the background normal tissue.
Conclusions: Finite element and tissue-mimicking phantom results demonstrate the feasibility of utilizing both the normalized axial-shear and full-shear strain area features to classify breast masses. Differentiation between bound or unbound masses was not affected by the mass size or shape for masses where the applied deformation is normal to the mass surface. Shear strain patterns vary significantly especially within unbound masses, when the mass surface is not normal to the applied deformation. Discrimination performance for unbound masses was improved by utilizing only the normalized shear strain area patterns located outside the mass as illustrated in this paper. [DOI: 10.1118/1.3651461]

Key words: ultrasound elastography, breast cancer, shear strain, finite element analysis, NASSA

I. INTRODUCTION

One out of eight women (12%) will be diagnosed with breast cancer during her life time in the United States, accounting for approximately 28% of all new cancer cases among women.[1,2] The primary goal of screening modalities is early detection of breast cancer. However, only 40% of the high-risk women undergo regular screening mammograms in the United States.[3] Of these patients, about 1.3%–2.5% also underwent a breast biopsy.[4,5] Unfortunately, the benign to malignant ratio for breast biopsies ranges from 5.0 to 0.2 for women in different age ranges, leading to more benign masses being biopsied.[4,5] Incorporating new noninvasive and nonionizing imaging features to further differentiate solid masses as benign could improve the early detection accuracy and thereby reduce unnecessary biopsies.

Both quasi-static[6–10] and dynamic[11–14] ultrasound elastography based approaches that are noninvasive and nonionizing modalities, show promise for the differentiation of benign from malignant breast masses.[6,15–18] Variations in the stiffness of breast masses in axial-strain images was initially used for differentiation,[15] followed by utilization of a size-discrepancy or size-ratio feature derived from the differences in the visualization of the breast mass on ultrasound B-mode and axial-strain images.[19–21] Use of additional features that utilize the bonding characteristics of breast masses to surrounding normal tissue have also been reported.[22–27] Since cancers infiltrate into surrounding normal tissue, they are far

less mobile and exhibit reduced slippage during deformation in contrast to benign masses like fibroadenomas that are not firmly attached to surrounding normal tissue.[22–27]

Shear strain imaging has been shown to provide new and additional novel features that can be utilized to differentiate benign breast masses (unbound) from malignant masses (bound).[22–24] The full-shear strain component includes contributions from both axial-shear and lateral-shear due to the applied deformation. However, many investigators utilize only the axial component of the estimated local displacements to generate axial-shear strain images,[25–27] while ignoring the contributions of the lateral-shear component.[22–24] This represents a practical solution since estimation of lateral displacements from radiofrequency (RF) data acquired along the 0° insonification or backscatter direction can be noisy leading to additional noise artifacts in the shear strain image.

Our laboratory has developed approaches that utilize angular displacements estimated using beam steering to estimate both axial and lateral displacements in response to an applied deformation. Techavipoo *et al.*[24] proposed an approach to obtain normal and shear strain tensors using RF echo data collected using phased array transducers, translated to obtain data along a scan plane. Rao *et al.*[28] implemented this approach using beam steering on a linear array transducer, along with one-dimensional (1D) cross-correlation based displacement tracking for the angular data sets. Both these approaches assumed that estimated displacement noise artifacts were independent and identically distributed, modeled using a zero-mean normal probability density function. Chen and Varghese[29] extended this analysis, eliminating assumptions on the angular displacement noise artifacts by incorporating them into the least-squares strain estimation using a cross-correlation matrix of the displacement noise artifacts.

Most of the previous analysis described in the literature has been performed with spherical inclusions or masses.[26] However, since most breast masses are not spherical and manifest as masses with different shapes, theoretical[30] and experimental[31] axial-shear strain patterns associated with cylindrical inclusions with an elliptical cross-section in tissue-mimicking (TM) phantoms have been reported. *In-vivo* examples of benign breast masses with ellipsoidal shapes and non-normal orientations to the scanning plane have also been discussed.[31] Analytic solutions of the elasticity distribution of bound ellipsoidal inclusions have also been previously described in the peer-reviewed literature.[32]

In-vivo results on breast masses demonstrating the use of "normalized area of the axial-shear strain regions" was first reported by Thittaikumar *et al.*[26] Changes in the normalization of the feature, primarily through utilization of breast mass dimensions obtained from the axial-strain image along with use of the acronym NASSA to denote the "normalized axial-shear strain area" feature was reported in Xu *et al.*[27] The NASSA feature has been utilized as a discriminant to classify breast masses as benign or malignant in the literature.[25–27]

In this paper, we use finite element analysis (FEA) software to model and evaluate both the normalized axial-shear strain area (NASSA) and the normalized full-shear strain area (NFSSA) features exhibited by different inclusion shapes (spherical and ellipsoidal masses) and for asymmetric positioning of ellipsoidal masses within an uniformly elastic background. Changes in the NASSA and NFSSA feature values for these inclusion shapes are presented for variations in the friction coefficient between the mass boundary and background tissue modeling the attachment of the mass to background tissue.[33] Different mass dimensions characterized by variations in the major (a) and minor (b) diameters of the mass, stiffness ratios, applied deformation and orientations of the mass with the background tissue are also studied. Simulation results are then corroborated using experimental TM phantoms with both symmetric and asymmetrically positioned ellipsoidal masses.

II. MATERIALS AND METHODS

II.A. Finite element model

Two-dimensional (2D) axisymmetric finite element simulations for both spherical and ellipsoidal masses embedded in a uniformly elastic background were modeled for shear strain imaging analysis using ANSYS (ANSYS Inc., Pittsburgh, PA) software. Since the simulation was performed in 2D, a cross-section of the ellipsoidal mass was modeled under plane strain conditions; referred to as an ellipse or elliptical model in our FEA simulations. The simulated FEA phantom model was fixed on the bottom surface to model the attachment of breast tissue to the chest wall, and was free to move on both sides. A "quasi-static" compressive deformation was then applied to the top surface of the phantom. The term quasi-static refers to the use of a uniaxial applied deformation that is not vibratory, enabling the use of the simpler Hookean equation $Kx = F_0$, where K denotes the stiffness matrix, x the displacement and F is the applied uniaxial deformation.[6,18,34] For the 2D model with the embedded spherical mass, a single-inclusion with a 10 mm diameter was embedded within a uniform background with dimensions 40×40 mm. In a similar manner, the 2D ellipsoidal mass model, utilized a single elliptical mass characterized by major (a along the x-direction) and minor (b along the y-direction) diameters of 12 and 9 mm, respectively, embedded within a uniformly elastic background.

A distinct boundary referred to as the contact interface was created along the inclusion embedded within background surrounding tissue to model the bonding of the inclusion surface and background tissue. Different degrees of bonding at the mass/background interface was modeled using friction coefficient values ranging from 0.01 to 100 depicting unbound to bound masses.[33] For modeling malignant masses, the inclusion was bound or attached to the surrounding medium, which was implemented in ANSYS by gluing (a friction coefficient value around 100 provides similar results) the contact surfaces together during the modeling step. The benign mass, on the other hand (unbound mass) was implemented in ANSYS by assigning a lower friction coefficient value to the contact interface elements at the boundary.

Two different tissue material types were utilized in the FEA model to simulate the TM phantom that includes both tumor and normal surrounding tissue. We assumed that both these tissue materials were isotropic, and homogeneous, requiring only two constants to describe the deformation response.[34] Young's modulus and Poisson's ratio. The Poisson's ratio for both the background and inclusion materials was set to 0.495 simulating incompressible tissue. The Young's modulus, on the other hand was set to different values for the tumor and the background based on the experimental results reported in the literature for breast tissue.[35] The ratio between the Young's modulus values of the inclusion and background represents their relative stiffness contrast. Since shear strain distributions are generated at the background/inclusion interface, we are more interested in the variation of these patterns at the interface or boundary of the inclusion. Thus, the meshed regions around these interfaces were assigned with a finer mesh density in order to obtain accurate lateral and axial displacement information from the FEA simulation. The pre- and postdeformation displacement information describing both the axial and lateral displacements were output from the ANSYS software and interpolated to a regular Cartesian grid using MATLAB (The Mathworks, Natick, RI). This interpolated data were utilized to evaluate the respective strain and shear strain distributions.

II.B. TM Phantom corroboration

Four single-inclusion TM phantoms each with a single ellipsoidal inclusion were studied to corroborate the mass differentiation performance between the axial-shear and full-shear features, respectively. An ellipsoidal mass with dimensions $(19 \times 14 \times 14)$ mm was embedded within the center of a uniform cubic background with dimensions $(80 \times 80 \times 80)$ mm for each phantom. The selection of the ellipsoidal mass dimensions was based on mass dimensions reported in *in-vivo* studies.[19–21,25–27] The acoustic and elastic properties of the TM materials used in the phantom and the phantom production procedure have been previously described in Madsen *et al.*[36,37] The Young's modulus values for the various materials in the phantoms were obtained using dynamic mechanical testing *via* an EnduraTEC ELF 3220 (Bose Corporation, EnduraTEC Systems Group, Minnetonka, MN). The Young's modulus values and contrasts (ratio of Young's moduli between the mass and background) are shown in Table I.

The ellipsoidal masses were positioned at the center of the cubic background material. For the phantoms with representations of benign ellipsoidal masses, a layer of petroleum jelly was applied around the masses before they were embedded in the uniformly elastic TM background. On the other hand, for the ellipsoidal masses that mimic malignant tumors, infiltration of the masses into the background was assured by "gluing" the masses to the previously congealed surrounding background material with molten TM background material. The phantoms with unbound ellipsoids (Phantoms 1 and 3) simulate a benign tumor with the symmetrically and asymmetrically oriented masses with stiffness values that are 4.2 and 3.2 times greater than the background material, respectively. Phantoms 2 and 4 also have a modulus contrast of 4.2 and 3.2, respectively, with respect to the background TM material. Application of the quasi-static deformation on different surfaces of the cubical phantom therefore provides different relative angles of the major axis to the applied deformation surface. Thus, for the ellipsoidal mass in the symmetrical phantoms (Phantom 1 where the ellipsoid was bound to the background material; representing a cancer, and Phantom 2 where the ellipsoid was unbound to the background material; representing a benign tumor), we evaluate shear strain patterns obtained along both the 0° and 90° orientation of the mass with the background. In a similar manner, for the phantoms with the asymmetrical mass, we evaluate shear strain patterns for both 30° and 60° orientations of the major axis of the mass with the background (Phantom 3 where the ellipsoid was bound to the background material and Phantom 4 where the ellipsoid was unbound to the background material).

The TM phantoms were scanned using a Siemens ACUSON S2000 real-time clinical scanner (Siemens Ultrasound, Mountain View, CA) equipped with a VFX 9L4 linear-array transducer operating at a 6 MHz center frequency. A single focal zone was selected at a depth of 40 mm, also located at the center of the phantom. RF data at a 40 MHz sampling frequency were acquired. The transducer was held in a motion controlled stage and embedded within a compressional plate to provide a uniform quasi-static deformation to the top surface of the phantom. A quasistatic deformation was applied on the top surface of the selected TM phantoms. In order to estimate lateral displacements, beam steering to obtain angular RF data ranging from −15° to 15° in increments of 1° were acquired. These beam steered pre- and postdeformation RF data were acquired before and after a deformation of 1% of the phantom height (0.8 mm) which was aided by positional stage as illustrated in Fig. 1. A compression plate larger than the dimensions of the TM phantom top surface was used to provide a uniform deformation.

TABLE I. Young's Modulus values of the TM phantom materials and their respective Modulus contrasts.

No.	Background dimension (mm)	Inclusion dimension (mm)	Angle	Bound/unbound	Young's Modulus (I/kPa)	Young's Modulus (B/kPa)	Contrast (I/B)
1	$40 \times 40 \times 40$	$19 \times 14 \times 14$	0°/90°	Unbound benign	48.0	11.3	4.2
2	$40 \times 40 \times 40$	$19 \times 14 \times 14$	0°/90°	Bound malignant	48.0	11.3	4.2
3	$40 \times 40 \times 40$	$19 \times 14 \times 14$	30°/60°	Unbound benign	58.7	18.2	3.2
4	$40 \times 40 \times 40$	$19 \times 14 \times 14$	30°/60°	Bound malignant	58.7	18.2	3.2

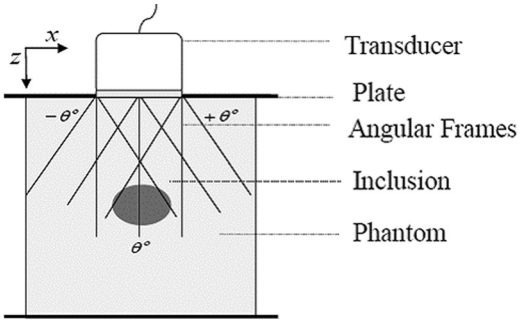

FIG. 1. Schematic diagram of RF data acquisition using a linear array transducer with beam steering. Note that z represents the direction of the applied deformation also referred to as the axial direction and x represents the lateral direction, respectively. The beam steered angle for insonification is varied from $-\theta^\circ$ to $+\theta^\circ$. A compression plate larger than the top surface of the phantom is used to provide a uniform deformation.

II.C. Displacement estimation

Angular displacements (displacement along beam direction) were estimated from pre- and post- deformation RF data pair along each beam steering angle using a 1D cross-correlation algorithm with 2D tracking of the displacement.[23] Angular displacements along each beam direction were separated into their axial- and lateral displacement components, respectively. A 1D cross-correlation algorithm was utilized, since 2D cross-correlation blocks have to be parallelogram shaped with an appropriate angle for the angular data sets. Efficient approaches to process angular data sets with 2D cross-correlation blocks have yet to be developed. Only median filtering was used to remove outliers in the angular displacement estimates obtained using 1D cross-correlation analysis with 2D motion tracking. In addition, only displacement estimates with a normalized cross-correlation coefficient value greater than 0.75 were used in the least-squares strain estimation. A window size of 3 mm along with a 75% overlap was used to perform displacement estimation using the RF data. However, since the angular displacements were estimated along each beam steering angle, they have different pixel grid locations. In order to make the angular displacement vectors amenable for image registration, they were interpolated onto the zero-angle spatial grid using bilinear interpolation. The axial- and lateral-displacement components were then estimated from the angular displacements using a least-squares approach previously described by Techavipoo et al. and Rao *et al.*[28,38]

II.D. Shear strain tensor estimation and normalization

Axial- and lateral- displacements interpolated to the zero-angle grid, and estimated from the beam steered RF data were utilized to calculate the axial-shear and full-shear strain tensor for comparison in this paper. The shear strain (or full-shear strain) tensor along the ultrasound scan plane is defined by

$$\text{Full} - \text{Shear Strain} = \frac{1}{2}\left(\frac{\partial d_z}{\partial x} + \frac{\partial d_x}{\partial z}\right),$$
$$e_{zx} = \frac{\partial d_z}{\partial x}, \quad e_{xz} = \frac{\partial d_x}{\partial z}. \tag{1}$$

where d_z and d_x represent the axial- and lateral displacement components in the zero-angle grid, respectively. The full-shear strain tensor includes both the axial-shear strain tensor (e_{zx})[26] and the lateral-shear strain tensor (e_{xz}).

Both the axial-shear strain tensor and full-shear strain tensor were calculated from the local displacement components using a least-squares strain estimator.[39] The shear strain tensor was further filtered by an adaptive median filter with dimensions of 5×3 pixels for the axial-shear strain tensor, 3×5 pixels for the lateral-shear and 3×3 pixels for full-shear strain tensor, respectively.

In order to utilize the shear strain area feature, we first have to normalize these shear strain areas for performing comparisons over different mass dimensions (since tumor mass dimensions vary across patients) and under different scanning conditions where the applied deformations may also vary. The stiffness ratio or contrast between the mass and background tissue was another factor utilized for normalization of the shear strain area. Normalized axial-shear strain regions first reported by Thittaikumar *et al.*[26] utilize mass dimensions or areas estimated from ultrasound B-mode images, which can be subjective and depend significantly on the operator's expertise. Stravos[40] reports in his book that most fibroadenomas are visualized as isoechoic and only two-thirds of the malignant masses appear as hypoechoic masses on ultrasound B-mode images. In our shear strain area normalizations coined NASSA in Xu *et al.*[27] and NFSSA for the full-shear strain area, we utilize mass dimensions estimated from the axial-strain image, where they are clearly visualized and can also be obtained using automated segmentation based approaches.[41–43] The previously reported normalized shear strain area feature, however, included shear strain regions that could occur both within and outside the breast mass.[26,27] To further differentiate shear strain patterns, those that occur outside the masses (OM) are denoted as NASSA_OM and those within masses (IM) are denoted by NASSA_IM as shown in Fig. 2. The normalized shear strain patterns shown in Fig. 2 were obtained using FEA simulations for unbound masses. Normalized shear strain areas visualized within breast masses denoted by NASSA_IM was previously described as "fill-in" by ThittaiKumar *et al.*[30,31] for only unbound masses They have also reported that the "fill-in"[30,31] depends on the mass orientation, with larger values obtained for unbound

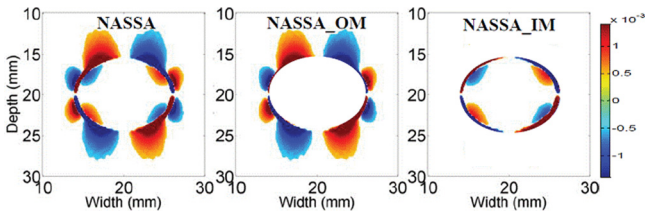

FIG. 2. Shear strain area mappings demonstrating the region mapped using the normalized axial-shear strain area (NASSA) (truncated from 10 to 30 mm) (a) The normalized shear strain area outside the mass (NASSA_OM) (b) and normalized shear strain area inside the mass (NASSA_ IM) (c) obtained using FEA simulations for an unbound mass with a friction coefficient of 0.2. A 1% shear strain corresponds to 0.01 on the colorbar.

masses oriented at an angle (asymmetric) to the applied deformation.

III. RESULTS

Shear strain images shown in Fig. 3 were obtained from both FEA simulations (i) and TM phantom based experimental results (ii) with the inclusions oriented at both 0° (a) and 60° (b) to the applied deformation. The red regions denote positive shearing strain while the regions in blue denote negative or shearing strains in the opposite direction. The direction of the shearing strain is identified relative to the direction of the applied deformation. A comparison of the shear strain patterns between axial-shear (top row) and full-shear (bottom row) is presented for ellipsoidal masses. Since the FEA simulations are 2D, a cross-section with an elliptical shape was utilized. Shear strain images are depicted for friction coefficient values of 0.2 and 10 denoting representative unbound and bound masses, respectively. Details on phantom construction for the experimental TM phantoms were presented in the previous section. Observe the distinct variations in the shear strain patterns between the bound and unbound masses: where (1) The "halo" (or larger strain value region) around the inclusion for the unbound mass no longer exists for the bound mass;[33] this concept was described previously in Rao *et al.*[33] for spherical inclusions under shear deformations. The presence of the "halo" was due to the presence of shearing forces on the inclusion when it was oriented at an angle to the applied deformation, and is another feature that can be used to differentiate between benign and malignant breast masses; (2) The magnitude of the normalized full-shear strain area patterns are slightly lower than that seen with axial-shear alone; (3) Normalized shear strain area patterns outside the breast masses (NASSA_OM and NFSSA_OM) appear to be larger for the bound mass[26] when compared to the unbound ones; (4) Normalized shear strain areas visualized inside breast masses denoted by NASSA_IM and NFSSA_IM, previously described as "fill-in"[30,31] for the unbound mass are not observed for the bound mass in both simulations and experiments; (5) The negative and positive shear strain area patterns also vary along the contact interface for asymmetric location of the mass in background tissue. This was also observed for the results obtained with the experimental TM phantoms in Fig. 3(ii). Symmetric shear strain patterns are observed for ellipsoidal inclusions oriented at 0° to the applied deformation surface as shown in Fig. 3, which was consistent with the results reported with the previous spherical inclusion studies.[22,27,31,44]

Shear strain images shown in Fig. 3 (ii) represent ellipsoidal TM phantom results oriented at 0° and 60° to the applied deformation. Note that the TM phantom results exhibit similar characteristics as those described for the FEA simulation results. However, the TM phantom results include additional noise artifacts around the bottom of the ellipsoidal masses, primarily due to the lower signal-to-noise ratio (SNR) associated with the echo signal and attenuation in the phantom. As shown in Fig. 3 (ii), both axial-shear strain and full-shear strain images exhibit lower SNR in regions below the center of the phantom. We therefore utilize shear strain estimates obtained in regions above the center of the phantom ($\leq$40 mm) for quantitative experimental analysis.

Previous studies based on spherical masses have demonstrated that a threshold set at 20% of the applied deformation provided an optimal value for the NASSA and NFSSA features. The threshold was obtained by multiplying the applied deformation and strain contrast by a fixed percentage value (see Fig. 4). Shear strain estimates with absolute values larger than this threshold and appropriately scaled to tumor dimensions were utilized to estimate the normalized NASSA or NFSSA feature values. The red regions on the shear strain image in Fig. 3 therefore represent shear strain estimates larger than the positive value of the threshold, while the blue regions represent shear strain estimates smaller than the negative threshold. Plots of both the NASSA [Fig. 4(a)] and NFSSA feature [Fig. 4(b)] with threshold values ranging from 10 to 40% in increments of 10% are shown in Fig. 4 for elliptical masses, for friction coefficient ranging from 0.01 to 100. Observe from Fig. 4, that a threshold of 20% of the applied deformation provides an optimal value for both NASSA and NFSSA features for differentiation between the modeled FEA elliptical inclusions consistent with the previously described results for spherical inclusions. Previously published *in-vivo* results[25,27] have reported on the use of NASSA features obtained utilizing a threshold level of 20%[27] and 25%, respectively.[25,26,30] In general, lower thresholds provide improved discrimination at the cost of increased noise in the shear strain features. The 20% threshold value is also used in this paper. Also note from Fig. 4, that NFSSA features provide a better differentiation between lower friction coefficient and high friction coefficient masses when compared to the NASSA feature.

Variations in the NASSA and NFSSA features values based on inclusion dimensions are shown in Figs. 5(a) and 5(b), versus the friction coefficient similar to that plotted in Fig. 4. Figure 5 presents three different inclusion dimensions characterized by the ratio of the minor to major diameter (b/a). The inclusion with a b/a value of 1 corresponds to a spherical inclusion. The NASSA feature value shows the same trend (i.e., the feature value saturates for lower friction coefficient values (unbound masses), increases linearly for friction coefficient values in the 0.5–10, range, while saturating again for friction coefficient values larger than 10) [Fig. 5(a)] for inclusions with different b/a. They also demonstrate a larger variance, along with a reduced difference between the two saturation levels when compared to the NFSSA feature shown in Fig. 5(b). Both features demonstrate low values for unbound inclusions that increase as the mass become progressively attached to the background tissue.

Variations in the feature values for changes in the stiffness contrast between the inclusion and background tissue are shown in Fig. 6. Three values of the background/inclusion ratio were studied, namely 1:3, 1:5, 1:10 to evaluate if stiffening of the inclusion would change the shear strain patterns. The Young's modulus of the background tissue was set to 10 kPa in our FEA analysis. Note

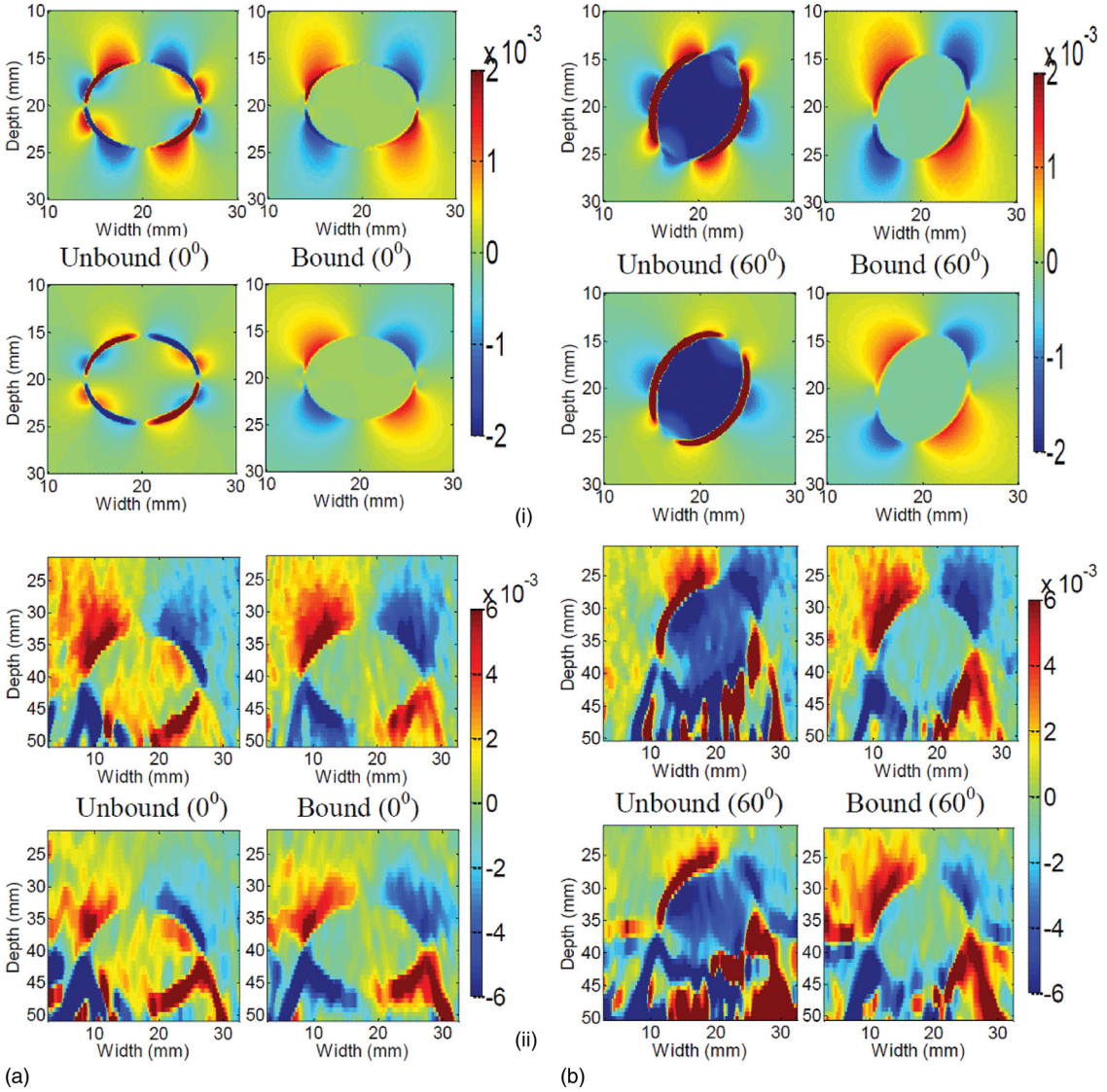

FIG. 3. Shear strain images obtained using FEA simulation (truncated from 10 to 30 mm) (i) and corresponding TM phantom experiments (truncated from 24 to 51 mm) (ii). Comparison of the shear strain patterns obtained using axial-shear (top row) to that obtained with full-shear (bottom row) for elliptical and ellipsoidal inclusions oriented at an angle of 0° (a) and 60° (b) to the applied deformation for different bonding conditions are shown. A 1% shear strain corresponds to 0.01 on the colorbar.

that these background/inclusion stiffness contrast ratios possess similar variations in the NASSA and NFSSA feature values as shown in Fig. 6. However, the difference between the NASSA and NFSSA feature values between the unbound to bound masses are larger for stiffer masses or those with an increased stiffness contrast (1:5 and 1:10). The increased difference obtained between the feature values for unbound to bound masses is significant, since we model benign masses as unbound while malignant masses are bound or attached to the background normal tissue through infiltration. A larger difference would enable improved discrimination between the benign and malignant breast masses. In

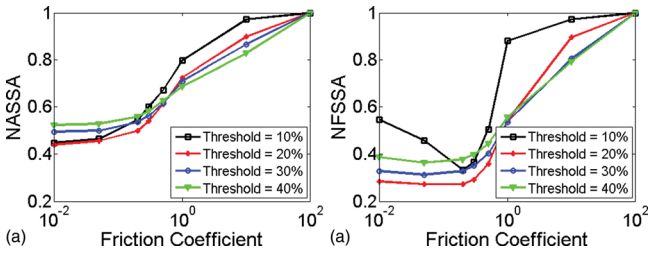

FIG. 4. Plots depicting variations in the NASSA and (a) NFSSA (b) for ellipsoidal inclusions for different threshold values obtained using FEA simulation.

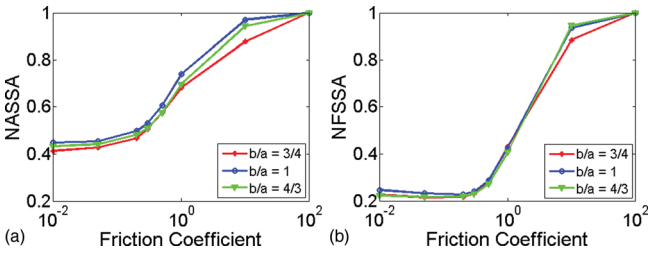

FIG. 5. Plots showing variations in the NASSA (a) and NFSSA (b) feature values for ellipsoidal inclusions with different b/a value obtained using FEA simulation.

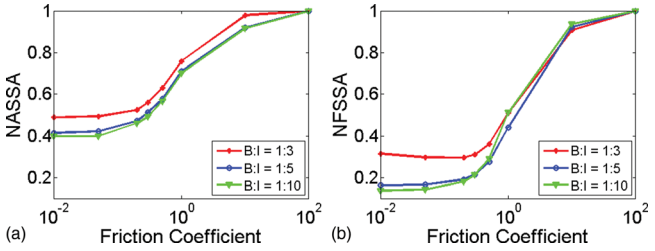

FIG. 6. Plots showing the impact of various stiffness ratio values on the NASSA (a) and NFSSA (b), respectively.

addition, note that the difference is larger for the NFSSA feature value, indicating that higher stiffness contrast improves discrimination with the use of the NFSSA feature. Variation in the features due to the applied deformation (AD) is shown in Fig. 7. Observe that both NASSA and NFSSA feature values with friction coefficient lower than 0.4 are unstable for larger applied deformation (>5%), probably due to increased mass slippage.

Finally, we evaluate the impact of inclusion orientation with respect to the applied deformation for both bound and unbound masses based on both FEA simulations [Figs. 8 and 9 (i)] and experimental TM phantom results [Figs. 8 and 9 (ii)]. For FEA simulation, we evaluate the impact of asymmetric inclusion orientation by rotating the elliptical inclusion from 0° to 90° in steps of 10° (relative to top surface of the model where the deformation is applied), assigning the unbound inclusions with a 0.5 friction coefficient value and gluing the contact interface of bound model together. For the TM phantom, both the NASSA and NFSSA quantitative feature values are extracted from the upper half of the corresponding shear strain image, respectively (above the phantom center (≤40mm)). The full-shear strain image was obtained by processing beam-steered RF data between ±15°. Since only four TM phantoms were constructed results are presented for the NASSA and NFSSA feature values for ellipsoidal inclusions oriented at 0°, 30°, 60°, and 90°, respectively, for both the bound and unbound phantoms. Observe that both the feature values, namely NASSA and NFSSA present with values that are larger along all orientation angles when compared to the unbound inclusion; also note that both the NASSA and NFSSA values vary significantly with orientation angle for the unbound mass, indicating that the asymmetric mass location with respect to the applied deformation may significantly impact the differentiation between bound and unbound masses. The best discrimination between bound and unbound masses was obtained for mass orientations of 0° and 90°, respectively. In addition, observe that the overall NFSSA feature values are lower than NASSA

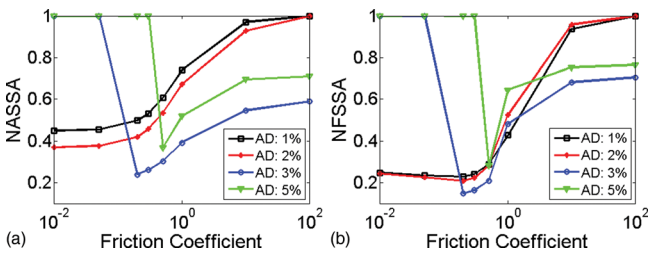

FIG. 7. Impact of applied deformation on NASSA (a) and NFSSA (b).

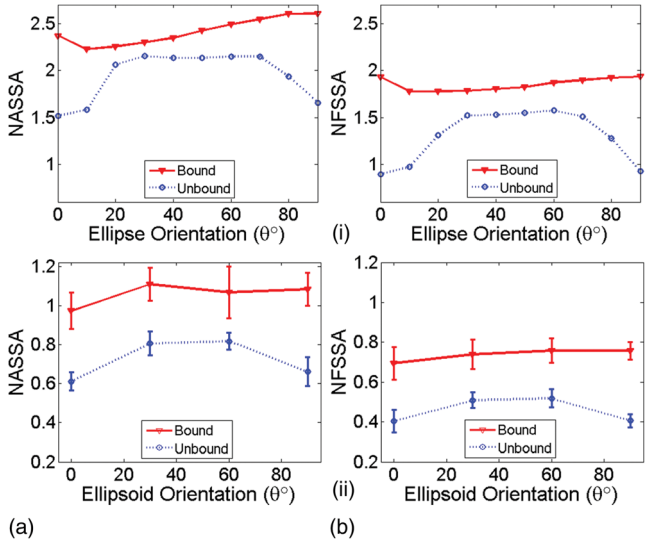

FIG. 8. Plots demonstrating the impact of inclusion orientation to the applied deformation for both FEA simulations (top row or i) and experimental TM phantom results (bottom row or ii). Column (a) demonstrates the variations in the NASSA feature values while column (b) presents the same for the NFSSA feature values. The error bars denote the standard deviation of the mean feature value estimated from ten independent sets of RF data acquired on the TM phantoms.

feature values both for FEA simulation results (i) and TM phantom results (ii) in Figs. 8 and 9.

Discrimination was worse when the mass was oriented at an angle due to the increased shear strains within these masses.[30,31] One way to circumvent this would be to apply deformations with the mass oriented at 0° or 90° to the applied deformation. Note that the NFSSA feature was more stable and constant for the bound inclusions when compared to the NASSA feature value as observed in the simulation results. The simulation results are based on 10 different

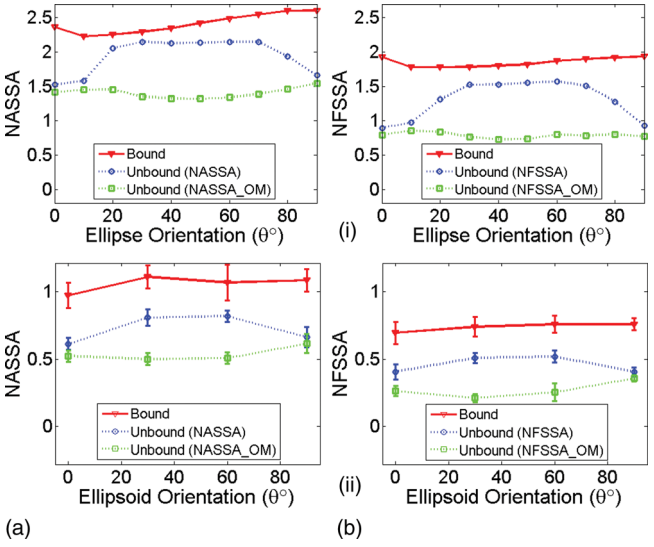

FIG. 9. Plots demonstrating the impact of inclusion orientation to the applied deformation with and without shearing strains within the inclusion for both FEA simulation (i) and experimental TM phantom results (ii). Column (a) demonstrates the variations in the NASSA feature values while column (b) presents NFSSA feature values. The error bars the standard deviation of the mean feature value estimated from ten independent sets of RF data acquired on the TM phantoms.

angular orientations of the mass, thereby providing more detail in the variation of the feature values with angle. On the other hand the experimental results in Fig. 8 (ii) are based on only four inclusion orientations and also include noise artifacts inherent with an experimental study. Therefore, the deviation between the bound and unbound inclusions at orientation of 30° and 60° are not as pronounced as that observed for the simulation results in Fig. 8 (i). Some of these artifacts are due to reduced averaging at the sides of the inclusion due to the reduced coverage with beam steered data collection and increased ultrasound noise artifacts. The error bars plotted in Figs. 8 and 9(ii) represent the standard deviation of the mean feature value (NASSA and NFSSA) estimated from ten independent sets of RF data acquired on the TM phantoms. Note that the standard deviation for the features derived from the unbound phantom was relatively smaller than that for the bound masses. Since shear strain patterns within the masses only exists for unbound or loosely bound masses, and specifically for asymmetric positioning of the masses, we plotted the NASSA_OM and NFSSA_OM feature values in Fig. 9. Note that NASSA_OM and NFSSA_OM were obtained by excluding any shear strain patterns within the inclusion or mass. As illustrated in Fig. 9, without accounting for shear strains within masses, both the NASSA_OM and NFSSA_OM features provide significantly better differentiation between benign and malignant masses for all asymmetric orientations of the mass with respect to the applied deformation. In addition, the NFSSA feature was more stable for unbound masses as shown in Fig. 9(b). Further analysis and additional features may be required to completely characterize masses that are oriented at an angle to the applied deformation.

IV. DISCUSSION AND CONCLUSIONS

In this paper, we show the feasibility of utilizing both the NASSA and the NFSSA feature to differentiate between benign or malignant breast masses based on their attachment to background tissue. Differentiation between bound or unbound masses was not affected by the lesion size or shape for symmetric positioning or location of the mass within the background. On the other hand, for unbound masses shear strains within the inclusion were enhanced especially with asymmetric positioning of masses within the background. For asymmetric masses, these shear strains within the inclusion introduce errors that reduce the ability of both the NASSA and NFSSA features to differentiate between firmly and loosely attached masses as shown in Fig. 9. Orientation of the mass at 0° or 90° to the applied deformation for data acquisition on patients would be an obvious solution as illustrated in Fig. 9. Another option as illustrated in this paper would be to exclude shear strains within the inclusion as illustrated with the use of the NASSA_OM and the NFSSA_OM features, respectively. Mass differentiation and classification between bound and unbound masses for all orientations with respect to the applied deformation was improved significantly by excluding shearing strains within the inclusion or mass. However, we have to keep in mind that the shearing strains within an inclusion could be an indicator of necrotic regions within a breast mass that could be significantly stiffer than the surrounding tissue, or perhaps an indicator of multiple distributed masses.[45]

Another artifact source are the tracking errors present with 1D cross-correlation based motion tracking, that introduce the signal decorrelation errors observed at increased depths in the phantom (for depths >5 cm in Fig. 3) due to lower ultrasound SNR associated with the echo signal and attenuation in the phantom. The reduced SNR introduce noise artifacts into both the NASSA and NFSSA features reducing their ability to differentiate between benign from malignant breast masses. Improved displacement tracking and estimation with 2D kernels, are therefore necessary to estimate angular displacements with improved accuracy and spatial resolution.

Results reported in the paper also indicate that increased mass stiffness improves classification using the NFSSA feature, when compared to the NASSA feature based on the larger difference in the feature values for bound or unbound masses shown in Fig. 6. In general increased mass stiffness with respect to background tissue improves visualization of the shearing strains. Finally, Fig. 7 also indicates that larger applied deformations may introduce instabilities due to mass slippage for both NASSA and NFSSA features for unbound masses.

ACKNOWLEDGMENTS

This work is supported in part by NIH Grant Nos. 5R21CA140939-02, 3R01CA112192-03S1, and 5R21EB010098-02.

[a]Author to whom correspondence should be addressed. Electronic mail: tvarghese@wisc.edu; Telephone: (608) 265-8797; Fax: (608) 262-2413.

[1]ACS, "Breast cancer overview," http://www.cancer.org/Cancer/Breast-Cancer/OverviewGuide/index (2010).
[2]A. Jemal, R. Siegel, J. Xu, and E. Ward, "Cancer statistics, 2010," Ca-Cancer J. Clin. **60**, 277–300 (2010).
[3]B. E. Sirovich and H. C. Sox, Jr., "Breast cancer screening," Surg. Clin. North Am. **79**, 961–990 (1999).
[4]K. Kerlikowske, R. Smith-Bindman, B. M. Ljung, and D. Grady, "Evaluation of abnormal mammography results and palpable breast abnormalities," Ann. Intern. Med. **139**, 274–284 (2003).
[5]D. Gur, L. P. Wallace, A. H. Klym, L. A. Hardesty, G. S. Abrams, R. Shah, and J. H. Sumkin, "Trends in recall, biopsy, and positive biopsy rates for screening mammography in an academic practice," Radiology **235**, 396–401 (2005).
[6]J. Ophir, I. Cespedes, H. Ponnekanti, Y. Yazdi, and X. Li, "Elastography: A quantitative method for imaging the elasticity of biological tissues," Ultrason. Imaging **13**, 111–134 (1991).
[7]M. O'Donnell, A. R. Skovoroda, B. M. Shapo, and S. Y. Emelianov, "Internal displacement and strain imaging using ultrasonic speckle tracking," IEEE Trans. Ultrason. Ferroelectr. Freq. Control **41**, 314–325 (1994).
[8]E. I. Céspedes, C. de Korte, A. F. van der Steen, C. von Birgelen, and C. T. Lancée, "Intravascular elastography: Principles and potentials," Semin Interv Cardiol. **2**, 55–62 (1997).
[9]J. C. Bamber, "Ultrasound elasticity imaging: Definition and technology," Eur. Radiol. **9**, S327–330 (1999).
[10]M. Bilgen and M. F. Insana, "Deformation models and correlation analysis in elastography," J. Acoust. Soc. Am. **99**, 3212–3224 (1996).
[11]K. J. Parker, S. R. Huang, R. A. Musulin, and R. M. Lerner, "Tissue response to mechanical vibrations for 'sonoelasticity imaging'," Ultrasound Med. Biol. **16**, 241–246 (1990).

[12]M. Fatemi and J. F. Greenleaf, "Application of radiation force in noncontact measurement of the elastic parameters," Ultrason. Imaging **21**, 147–154 (1999).
[13]K. Nightingale, M. S. Soo, R. Nightingale, and G. Trahey, "Acoustic radiation force impulse imaging: in vivo demonstration of clinical feasibility," Ultrasound Med. Biol. **28**, 227–235 (2002).
[14]L. Sandrin, S. Catheline, M. Tanter, X. Hennequin, and M. Fink, "Time-resolved pulsed elastography with ultrafast ultrasonic imaging," Ultrason. Imaging **21**, 259–272 (1999).
[15]B. S. Garra, E. I. Cespedes, J. Ophir, S. R. Spratt, R. A. Zuurbier, C. M. Magnant, and M. F. Pennanen, "Elastography of breast lesions: initial clinical results," Radiology **202**, 79–86 (1997).
[16]K. M. Hiltawsky, M. Kruger, C. Starke, L. Heuser, H. Ermert, and A. Jensen, "Freehand ultrasound elastography of breast lesions: clinical results," Ultrasound Med. Biol. **27**, 1461–1469 (2001).
[17]T. J. Hall, Y. Zhu, and C. S. Spalding, "in vivo real-time freehand palpation imaging," Ultrasound Med. Biol. **29**, 427–435 (2003).
[18]T. Varghese, "Quasi-static ultrasound elastography," Ultrasound Clin. **4**, 323–338 (2009).
[19]E. S. Burnside, T. J. Hall, A. M. Sommer, G. K. Hesley, G. A. Sisney, W. E. Svensson, J. P. Fine, J. Jiang, and N. J. Hangiandreou, "Differentiating benign from malignant solid breast masses with US strain imaging," Radiology **245**, 401–410 (2007).
[20]D. M. Regner, G. K. Hesley, N. J. Hangiandreou, M. J. Morton, M. R. Nordland, D. D. Meixner, T. J. Hall, M. A. Farrell, J. N. Mandrekar, W. S. Harmsen, and J. W. Charboneau, "Breast lesions: Evaluation with US strain imaging–clinical experience of multiple observers," Radiology **238**, 425–437 (2006).
[21]R. G. Barr, "Real-time ultrasound elasticity of the breast: initial clinical results," Ultrasound Q **26**, 61–66 (2010).
[22]E. E. Konofagou, T. Harrigan, and J. Ophir, "Shear strain estimation and lesion mobility assessment in elastography," Ultrasonics **38**, 400–404 (2000).
[23]M. Rao, Q. Chen, H. Shi, T. Varghese, E. L. Madsen, and J. A. Zagzebski, "Normal and shear strain estimation using beam steering on linear-array transducers," Ultrasound Med. Biol. **33**, 57–66 (2007).
[24]U. Techavipoo, Q. Chen, T. Varghese, and J. Zagzebski, "Estimation of displacement vectors and strain tensors in elastography using angular insonifications," IEEE Trans. Med. Imaging **23**, 1479–1489 (2004).
[25]A. Thitaikumar, L. M. Mobbs, C. M. Kraemer-Chant, B. S. Garra, and J. Ophir, "Breast tumor classification using axial shear strain elastography: A feasibility study," Phys Med Biol **53**, 4809–4823 (2008).
[26]A. Thitaikumar, T. A. Krouskop, B. S. Garra, and J. Ophir, "Visualization of bonding at an inclusion boundary using axial-shear strain elastography: a feasibility study," Phys. Med. Biol. **52**, 2615–2633 (2007).
[27]H. Xu, M. Rao, T. Varghese, A. Sommer, S. Baker, T. J. Hall, G. A. Sisney, and E. S. Burnside, "Axial-shear strain imaging for differentiating benign and malignant breast masses," Ultrasound Med. Biol. **36**, 1813–1824 (2010).
[28]M. Rao, Q. Chen, H. Shi, T. Varghese, E. L. Madsen, J. A. Zagzebski, and T. A. Wilson, "Normal and shear strain estimation using beam steering on linear-array transducers," Ultrasound Med. Biol. **33**, 57–66 (2007).
[29]H. Chen and T. Varghese, "Noise analysis and improvement of displacement vector estimation from angular displacements," Med. Phys. **35**, 2007–2017 (2008).
[30]B. Galaz, A. K. Thittai, and J. Ophir, *8th International conference Ultrasonic Measurement and Imaging of Tissue Elasticity* (Vlissingen, Zeeland, Netherlands, 2009).
[31]A. K. Thittai, B. Galaz, and J. Ophir, "Axial-shear strain distributions in an elliptical inclusion model: experimental validation and in vivo examples with implications to breast tumor classification," Ultrasound Med. Biol. **36**, 814–820 (2010).
[32]J. D. Eshelby, "The determination of the elastic field of an ellipsoidal inclusion, and related problems," Proc. R. Soc. London, Ser. A **241**, 376–396 (1957).
[33]M. Rao, T. Varghese, and E. L. Madsen, "Shear strain imaging using shear deformations," Med. Phys. **35**, 412–423 (2008).
[34]J. Ophir, S. K. Alam, B. Garra, F. Kallel, E. Konofagou, T. Krouskop, and T. Varghese, "Elastography: ultrasonic estimation and imaging of the elastic properties of tissues," Proc. Inst. Mech. Eng., Part H: J. Eng. Med. **213**, 203–233. (1999).
[35]T. A. Krouskop, T. M. Wheeler, F. Kallel, and T. Hall, "Elastic moduli of breast and prostate tissues under compression," Ultrason. Imaging **20**, 260–274 (1998).
[36]E. L. Madsen, M. A. Hobson, H. Shi, T. Varghese, and G. R. Frank, "Stability of heterogeneous elastography phantoms made from oil dispersions in aqueous gels," Ultrasound Med. Biol. **32**, 261–270 (2006).
[37]E. L. Madsen, M. A. Hobson, G. Frank, H. Shi, J. Jiang, T. J. Hall, T. Varghese, M. M. Doyley, and J. B. Weaver, "Anthropomorphic breast phantoms for testing elastography systems," Ultrasound Med. Biol. **32**, 857–874 (2006).
[38]U. Techavipoo, Q. Chen, T. Varghese, and J. A. Zagzebski, "Estimation of displacement vectors and strain tensors in elastography using angular insonifications," IEEE Trans. Med. Imaging **23**, 1479–1489 (2004).
[39]F. Kallel and J. Ophir, "A least-squares strain estimator for elastography," Ultrason. Imaging **19**, 195–208 (1997).
[40]A. T. Stavros, in *Breast Ultrasound* (Lippincott Williams & Wilkins, Philadelphia, PA, 2004), Vol. 7, p. 95.
[41]W. Liu, J. A. Zagzebski, T. Varghese, C. R. Dyer, U. Techavipoo, and T. J. Hall, "Segmentation of elastographic images using a coarse-to-fine active contour model," Ultrasound Med. Biol. **32**, 397–408 (2006).
[42]U. Techavipoo, T. Varghese, J. A. Zagzebski, Q. Chen, and W. Liu, "Semiautomated thermal lesion segmentation for three-dimensional elastographic imaging," Ultrasound Med. Biol. **30**, 655–664 (2004).
[43]M. Zhang, B. Castaneda, J. Christensen, W. E. Saad, K. Bylund, K. Hoyt, J. G. Strang, D. J. Rubens, and K. J. Parker, "Real-time sonoelastography of hepatic thermal lesions in a swine model," Med. Phys. **35**, 4132–4141 (2008).
[44]M. Rao, "Shear Strain Elastography for Breast Cancer Diagnosis," Doctoral Dissertation, Thesis, University of Wisconsin-Madison, 2008.
[45]B. S. Garra, "Imaging and estimation of tissue elasticity by ultrasound," Ultrasound Q **23**, 255–268 (2007).